Eur. Phys. J. C (2023) 83:1004
https://doi.org/10.1140/epjc/s10052-023-12137-y

THE EUROPEAN PHYSICAL JOURNAL C

Regular Article - Experimental Physics

# Production of antihydrogen atoms by 6 keV antiprotons through a positronium cloud

**P. Adrich[1], P. Blumer[2], G. Caratsch[2], M. Chung[3], P. Cladé[4], P. Comini[5], P. Crivelli[2], O. Dalkarov[6], P. Debu[5], A. Douillet[4,7], D. Drapier[4], P. Froelich[8,21], N. Garroum[4,22], S. Guellati-Khelifa[4,9], J. Guyomard[4], P.-A. Hervieux[10], L. Hilico[4,7], P. Indelicato[4], S. Jonsell[8], J.-P. Karr[4,7], B. Kim[11], S. Kim[12], E.-S. Kim[13], Y. J. Ko[11], T. Kosinski[1], N. Kuroda[14], B. M. Latacz[5,23], B. Lee[12], H. Lee[12], J. Lee[11], E. Lim[13], L. Liszkay[5], D. Lunney[15], G. Manfredi[10], B. Mansoulié[5], M. Matusiak[1], V. Nesvizhevsky[16], F. Nez[4], S. Niang[15,23], B. Ohayon[2], K. Park[11,12], N. Paul[4], P. Pérez[5,a], C. Regenfus[2], S. Reynaud[4], C. Roumegou[15], J.-Y. Roussé[5], Y. Sacquin[5], G. Sadowski[5], J. Sarkisyan[2], M. Sato[14], F. Schmidt-Kaler[17], M. Staszczak[1], K. Szymczyk[1], T. A. Tanaka[14], B. Tuchming[5], B. Vallage[5], A. Voronin[6], D. P. van der Werf[18], A. Welker[19,24], D. Won[12], S. Wronka[1], Y. Yamazaki[20], K.-H. Yoo[3], P. Yzombard[4]**

[1] National Centre for Nuclear Research (NCBJ), ul. Andrzeja Soltana 7, 05-400 Otwock, Swierk, Poland
[2] Institute for Particle Physics and Astrophysics, ETH Zurich, 8093 Zurich, Switzerland
[3] Department of Physics, Ulsan National Institute of Science and Technology (UNIST), 50, UNIST-gil, Ulsan 44919, Republic of Korea
[4] Laboratoire Kastler Brossel, Sorbonne Université, CNRS, ENS-Université PSL, Collège de France, Campus Pierre et Marie Curie, 4, Place Jussieu, 75005 Paris, France
[5] IRFU, CEA, Université Paris-Saclay, 91191 Gif-sur-Yvette, France
[6] Affiliated with an Institute Covered by a Cooperation Agreement with CERN, Geneva, Switzerland
[7] Université d'Evry-Val d'Essonne, Université Paris-Saclay, Boulevard François Mitterand, 91000 Evry, France
[8] Department of Physics, Stockholm University, 10691 Stockholm, Sweden
[9] Conservatoire National des Arts et Métiers, 292 rue Saint Martin, 75003 Paris, France
[10] Université de Strasbourg, CNRS, Institut de Physique et Chimie des Matériaux de Strasbourg UMR 7504, 67000 Strasbourg, France
[11] Center for Underground Physics, Institute for Basic Science, 70 Yuseong-daero 1689-gil, Yuseong-gu, Daejeon 34047, Republic of Korea
[12] Department of Physics and Astronomy, Seoul National University, 1 Gwanak-ro, Gwanak-gu, Seoul 08826, Republic of Korea
[13] Department of Accelerator Science, Korea University Sejong Campus, Sejong-ro 2511, Sejong 30019, Republic of Korea
[14] Institute of Physics, University of Tokyo, 3-8-1 Komaba, Meguro, Tokyo 153-8902, Japan
[15] Université Paris-Saclay, CNRS/IN2P3, IJCLab, Orsay, France
[16] Institut Max von Laue-Paul Langevin (ILL), 71 avenue des Martyrs, 38042 Grenoble, France
[17] QUANTUM, Institut für Physik, Johannes Gutenberg Universität, 55128 Mainz, Germany
[18] Department of Physics, Faculty of Science and Engineering, Swansea University, Swansea SA2 8PP, UK
[19] CERN, Esplanade des Particules 1, 1217 Meyrin, Switzerland
[20] Ulmer Fundamental Symmetries Laboratory, RIKEN, 2-1 Hirosawa, Wako, Saitama 351-0198, Japan
[21] *Present address* Ångström Laboratory, Department of Chemistry, Uppsala University, Box 523, 75120 Uppsala, Sweden
[22] *Present address* LPNHE/IN2P3, 4, place Jussieu, 75252 Paris, France
[23] *Present address* CERN, Esplanade des Particules 1, 1217 Meyrin, Switzerland
[24] *Present address* 6300, Zug, Switzerland

Received: 8 July 2023 / Accepted: 13 October 2023
© The Author(s) 2023, corrected publication 2023

**Abstract** We report on the first production of an antihydrogen beam by charge exchange of 6.1 keV antiprotons with a cloud of positronium in the GBAR experiment at CERN. The 100 keV antiproton beam delivered by the AD/ELENA facility was further decelerated with a pulsed drift tube. A 9 MeV electron beam from a linear accelerator produced a low energy positron beam. The positrons were accumulated in a set of two Penning–Malmberg traps. The positronium target cloud resulted from the conversion of the positrons extracted from the traps. The antiproton beam was steered onto this positronium cloud to produce the antiatoms. We observe an excess over background indicating antihydrogen production with a significance of 3–4 standard deviations.

## 1 Introduction

The GBAR experiment at CERN aims at a precise measurement of the free fall acceleration of neutral antihydrogen

[a] e-mail: patrice.perez@cern.ch (corresponding author)

atoms in the terrestrial gravitational field, thus testing the Weak Equivalence Principle with antimatter. The antimatter atoms must be cooled to $\mu$K temperatures (i.e. $\sim 1\ \mathrm{m\,s^{-1}}$ velocities) to measure their free fall. The plan is to follow the original idea of Walz and Hänsch [1]. In this scheme, an anti-ion ( $\overline{\mathrm{H}}^{+}$) is first produced and sympathetically cooled with laser cooled $\mathrm{Be}^{+}$ ions. After photo-detachment at threshold, an ultra-cold anti-atom is produced. In order to obtain the anti-ions, two consecutive charge exchange reactions on positronium (Ps) are needed. In the first reaction, an antiproton beam interacts with a cloud of Ps to produce antihydrogen atoms, whereas in the second reaction those anti-atoms interact with another Ps from the cloud to form the antihydrogen ion [2].

The production of antihydrogen was first demonstrated in 1996 by the PS210 experiment at the CERN LEAR ring where 1.94 GeV/c antiprotons produced $e^{+}e^{-}$ pairs in a Xe target: $\overline{\mathrm{p}} + \mathrm{Z} \rightarrow \overline{\mathrm{p}}\ \gamma\gamma\ \mathrm{Z} \rightarrow \overline{\mathrm{p}}\ \mathrm{e}^{+}\mathrm{e}^{-}\ \mathrm{Z} \rightarrow \overline{\mathrm{H}}\ \mathrm{e}^{-}\ \mathrm{Z}$ [3]. In 1998, the E862 experiment at Fermilab used a high energy beam of 5.2 - 6.2 GeV/c antiprotons on a hydrogen gas jet target and the reaction: $\mathrm{p} + \overline{\mathrm{p}} \rightarrow \overline{\mathrm{H}} + \mathrm{e}^{-} + \mathrm{p}$ [4]. These experiments produced a few high energy anti-atoms. In 2002, the ATHENA and ATRAP collaborations at the CERN antiproton decelerator facility succeeded in producing sub-eV antihydrogen atoms [5,6]. In 2010 the ALPHA collaboration was able to catch about 38 $\overline{\mathrm{H}}$ atoms in a magnetic octupole trap, superimposed on a one tesla magnetic field [7]. The trap depth for ground state antihydrogen was about 0.5 K. The same year, the ASACUSA collaboration reported production using a CUSP trap [8] in order to produce a very low energy beam of $\overline{\mathrm{H}}$ (50 K temperature), which has been partially demonstrated [9].

The main formation mechanism involved in these trap experiments is a three-body reaction with one antiproton and two positrons, the second positron carrying away the excess energy released from the formation of the antihydrogen atom. Such a process is very efficient at producing several tens of anti-atoms per cycle that can be trapped as shown by the ALPHA collaboration [10]. In 2004 the ATRAP collaboration demonstrated another method involving positronium (Ps) itself produced by the interaction of positrons with excited Cesium atoms, in two resonant charge exchange reactions: $\mathrm{Cs}^{*} + \mathrm{e}^{+} \rightarrow \mathrm{Ps}^{*} + \mathrm{Cs}^{+}$ followed by $\mathrm{Ps}^{*} + \overline{\mathrm{p}} \rightarrow \overline{\mathrm{H}}^{*} + \mathrm{e}^{-}$ [11]. Here the third body is the electron from Ps. In 2021 the AEgIS collaboration reported the pulsed production of antihydrogen atoms in Rydberg states via the interaction of trapped antiprotons with Rydberg Ps [12]: $\mathrm{Ps}^{*} + \overline{\mathrm{p}} \rightarrow \overline{\mathrm{H}}^{*} + \mathrm{e}^{-}$.

In this work we present the experimental realisation of the first step of our scheme where a beam of antiprotons of 6.1 keV energy interacts with a cloud of Ps in the fundamental state, producing anti-atoms in the form of a pulsed beam according to reaction:

$$\overline{\mathrm{p}} + \mathrm{Ps} \rightarrow \overline{\mathrm{H}} + \mathrm{e}^{-} \tag{1}$$

where $\overline{\mathrm{p}}$ stands for antiproton and $\overline{\mathrm{H}}$ for antihydrogen.

The charge conjugated process of reaction (1) was measured in 1997 using a beam of 11.3 to 15.8 keV protons colliding with Ps [13] and producing hydrogen atoms with cross sections in the $10^{-15}$ cm$^2$ range. However, the precision on the measurement did not allow to settle the disagreement between the various atomic physics models reported in [13]. These models, along with more recent calculations [14–16], predict in any case that the cross sections should be higher at lower energy and exhibit a maximum in the range 6 to 10 keV. Moreover, the production of antihydrogen ions, which is the next step of the GBAR scheme, is most efficient when the antihydrogen is in its ground state. The corresponding cross sections are also higher at lower energy, towards the reaction thresholds [17]. Assuming that positronium and antihydrogen are in their ground states, the threshold is 5.6 keV and this is a further motivation for reducing the antiproton beam energy close to 6 keV.

Reaction (1) using ground state positronium produces antihydrogen atoms in low excited states, with 14% [15] to 22% [16] directly in the ground state, and the majority in the 2P state that rapidly decay to the ground state (lifetime of 1.6 ns). Compared to antiproton mixing with positrons in nested traps or with highly excited states of Ps, the present method is well suited for ground state antihydrogen production and therefore to subsequent antihydrogen ion formation.

In the following sections we first describe the main parts of the apparatus, and how we determine the number of Ps atoms and antiprotons participating in reaction (1) for each ELENA pulse. We then explain the method used to detect the produced atoms and reject the background, and how the resulting signal is obtained.

## 2 Experimental setup

A brief overview of the different parts of the apparatus is given here and illustrated schematically in Fig. 1. The antiprotons are delivered by the CERN AD-ELENA facility [18] at an energy of 100 keV, typically every 110 s. The $\overline{\mathrm{p}}$ bunch is decelerated with a drift tube [19] and directed towards the Ps target located in the reaction chamber (RC). A linear accelerator produces electrons that impinge upon a tungsten target equipped with a tungsten mesh moderator. The outcoming low energy positrons [20] are guided to the Penning–Malmberg traps. A buffer-gas trap (BGT) catches and cools the positron bunches. The $\mathrm{e}^{+}$ are then transferred to a high-field trap (HFT) where they are accumulated [21]

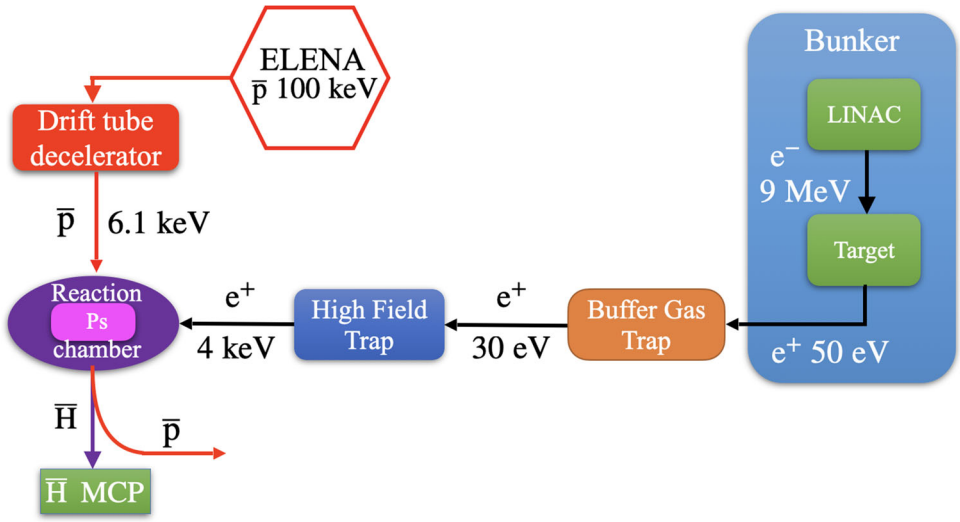


**Fig. 1** Scheme of the experiment. The positrons from the linac based source are accumulated in a set of two traps and directed to the reaction chamber where they are converted into positronium. Antiprotons from ELENA are decelerated with a drift tube and guided to the Ps target. The produced antihydrogen atoms are detected with an MCP while the antiprotons that did not react with Ps are deflected

between two $\bar{p}$ pulses and ejected towards the reaction chamber.

In the RC the $e^+$ are converted into a cloud of ortho-positronium (oPs), the triplet spin state with a lifetime of 142 ns, which serves as the target for the $\bar{p}$ to produce $\bar{H}$ atoms. The neutral anti-atoms hit a Micro Channel Plate (MCP) detector located in a straight line with respect to the incident $\bar{p}$ beam. This is our main device to detect $\bar{H}$. It will be denoted as $\bar{H}$ MCP in the following and described in detail in Sect. 5. The antiprotons that did not participate to the reaction are deflected away from the detector. Details on the production of the positronium target and on the antiproton beam are given in the two following sections.

## 3 Production of the positronium target

The positron beam is produced using a 9 MeV electron linear accelerator equipped with a water cooled tungsten target [20]. The peak electron current is 330 mA, with a pulse length of 2.85 μs. The repetition rate can be varied from 2 to 300 Hz. The high energy positrons (average 1 MeV) produced by pair creation in the 1 mm thick tungsten target are moderated to typically 3 eV (the work function of $e^+$ in W) in a series of tungsten meshes located beneath the target and accelerated to 50 eV for further transport in the beam line [20]. The slow positron flux is $2.9 \times 10^7$ per second.

A schematic of the positron beamline with the key components is shown in Fig. 2. The first element is an electrostatic repeller to reject electrons. The BGT captures and cools the positrons using $N_2$ ($10^{-4}$ mbar pressure) and $CO_2$ ($5 \times 10^{-5}$ mbar pressure) in a magnetic field of the order of 40 mT. It contains three stages of coaxial cylindrical electrodes. We apply voltages in the 30-140 V range to form potential wells to trap the positrons and dynamically transfer them along this setup. Positrons are transferred at 1 Hz repetition rate to the HFT where they are accumulated in a 5 T field in a vacuum better than $10^{-10}$ mbar. The cooling time by synchrotron radiation in this field is 0.16 s. The electrode stack consists of 27 electrodes in a 1.88 m long assembly. Typically 90 positron bunches from the BGT are accumulated by opening and closing the entrance potential barrier of the potential well at the 1 Hz frequency. Details of the trapping schemes can be found in reference [21].

The positron pulses, ejected at 300 or 500 eV from the HFT, are imaged with an MCP that can be moved in and out the beam line. The deposited charge can be measured using a fast charge sensitive pre-amplifier [22], while the front face of this MCP is biased at + 120 V to collect secondary electrons. The average number of positrons observed from the HFT was $1.5 \times 10^8$ per ELENA pulse. The overall efficiency of the system of the two traps is 5%.

Ideally, the magnetic field in the antiproton transport line should be zero. However, the 5 Tesla magnet of the HFT produces a fringe field of about 2 mT at the crossing of the beam lines in the RC. Thus a magnetic shielding box was installed consisting of 3 mm thick soft iron around the target location, reducing the field intensity at the target from 2 mT to about 0.4 mT. An extra layer of iron bars was added to increase the thickness of the magnet return yoke of the HFT. This reduces the fringe field to about 0.2 mT in the interaction zone. The positron beam traverses the 3 mm shielding wall via a 40 mm diameter hole located at 161 cm from the trap centre. The transition to the field-free region is made non-adiabatically to prevent the divergence of the positron beam [23].

Just before this transition, the positrons are further accelerated with a switched drift tube accelerator so that their final energy is 4.3 keV. This energy facilitates the transport into the magnetic field free zone where the positron beam is focused using a set of 100 mm diameter cylindrical electrodes (Fig. 3) and two planar electrodes to shape the beam so as to optimize

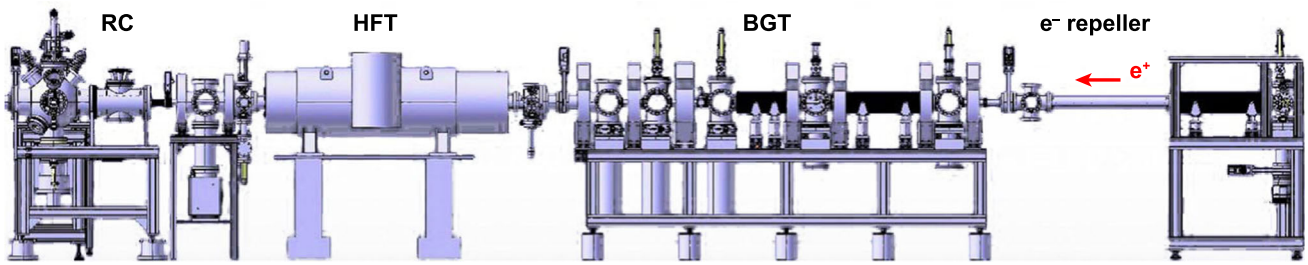


**Fig. 2** Side view of the 9.5 m long transport line of positrons from the linac (right, not shown) to the reaction chamber (RC at extreme left), with the electron repeller, the buffer-gas trap (BGT) and the high-field trap (HFT) in between

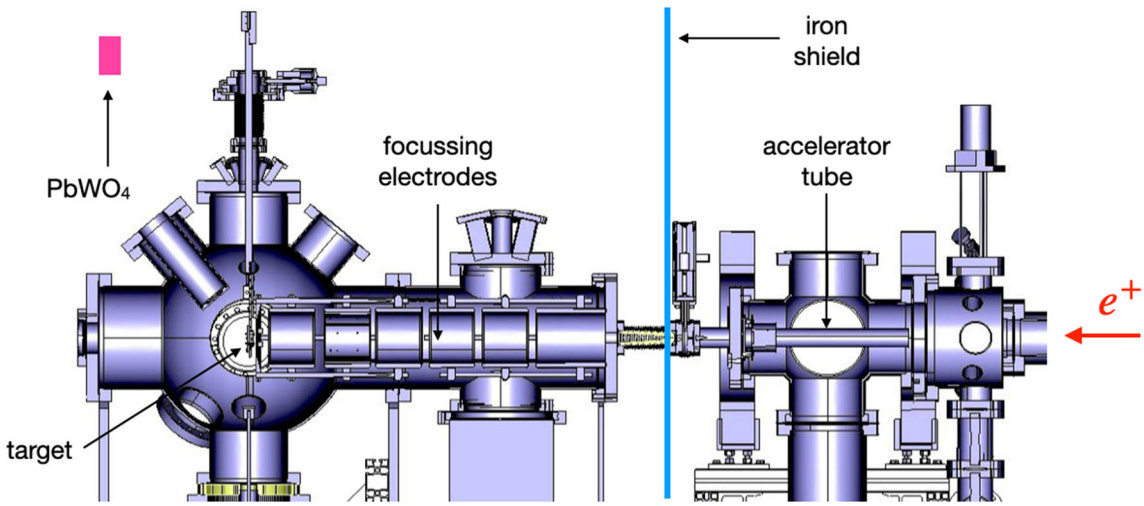


**Fig. 3** Side view of the transport of positrons to the Ps target. The HFT at the right ejects its stored positrons to the accelerator tube. The vertical blue line represents the iron wall of the magnetic shielding box. Six cylindrical electrodes focus the beam to the target position at the centre of the spherical reaction chamber where they are converted into Ps. A $PbWO_4$ crystal (pink) is placed close to the interaction point

the overlap with the antiproton beam profile in the interaction region. At the beam axes crossing point in the reaction chamber, the positron bunch is 17 ns (FWHM) long and its arrival time is set 30 ns earlier than the arrival time of the $\overline{p}$ bunch. This delay between particle bunches was found in simulations to be optimal for $\overline{H}$ production.

A sample holder, located at the centre of the RC, holds a flat 19 mm × 19 mm plate made of conductive silicon single crystal, on which a nanoporous silica film was deposited [24, 25]. At 4.3 keV the positrons are implanted deep enough in this Ps converter for ortho-positronium (oPs) to be emitted at low energy. Only oPs with a 142 ns lifetime has a chance to interact with an antiproton for $\overline{H}$ production whereas para-positronium, which has a lifetime of 125 ps, does not leave this film.

On the sample holder, another plate of the same dimensions as the Ps converter can be placed at the same location for reference. It is made of silicon and does not produce oPs. At a third position on the sample holder, an image sensitive 10 mm diameter MCP can also be moved to intersect the positron beam to check its focusing as sketched in Fig. 4. Using this MCP, the number of positrons reaching the RC is measured in a similar way as at the exit of the HFT with the same charge sensitive pre-amplifier. On average $5.2 \pm 0.5 \times 10^7$ $e^+$ per pulse reach the target plane, i.e. a 35% transport efficiency, with variations depending on the running conditions from 4 to $7 \times 10^7$ $e^+$. A measure of the overlap of the positron bunch with the antiproton beam is given by the fraction of positrons in a rectangle of 19 mm (the length of the Ps converter) by 5 mm (the diameter of the aperture of the collimator shown in Fig. 4), which is $73 \pm 3$ %.

A $4 \times 4 \times 3.8$ cm$^3$ $PbWO_4$ single crystal scintillator coupled to a fast photomultiplier (Hamamatsu H7195) detects the gamma rays emitted by the annihilation of the positrons hitting the target plane and by the decay of oPs. To estimate the fraction of oPs produced, we adapted the Single Shot Positron Annihilation Lifetime Spectroscopy (SSPALS) technique [26] by measuring the scintillation pulse after implantation of a large number of positrons in a short pulse. On average, a two-photon or three-photon annihilation event will deposit the same energy in the scintillator, as the detection efficiency is independent of the photon energy in the

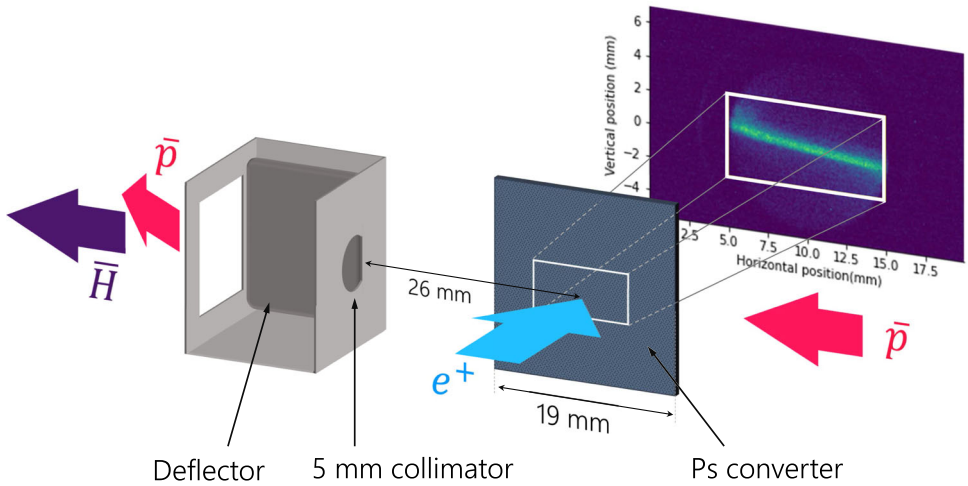


**Fig. 4** Schematic of the silica target region. An electrostatic deflector is located on the beam axis with its 5 mm diameter aperture 26 mm downstream the target centre acting also as a collimator. The positron beam profile seen by the MCP when placed at the same location as the Ps converter is also shown.The white rectangle figured on the screen has a length of 10 mm and a height of 5 mm

large scintillator crystal with high density. The long oPs annihilation component can be then estimated by deconvolution, using the pulse shape measured on a non-positronium emitting target, the silicon plate, as an instrumental function. We find that $18 \pm 3$ % of those positrons are converted into oPs (Fig. 5), resulting, on average, in $6.8 \pm 1.5 \times 10^6$ oPs created in the 19 mm × 5 mm rectangle.

This is thus the number of Ps atoms created for each ELENA pulse within a volume delimited by the collimator and this rectangle. In the next section we describe how we prepare the $\bar{p}$ component for the reaction.

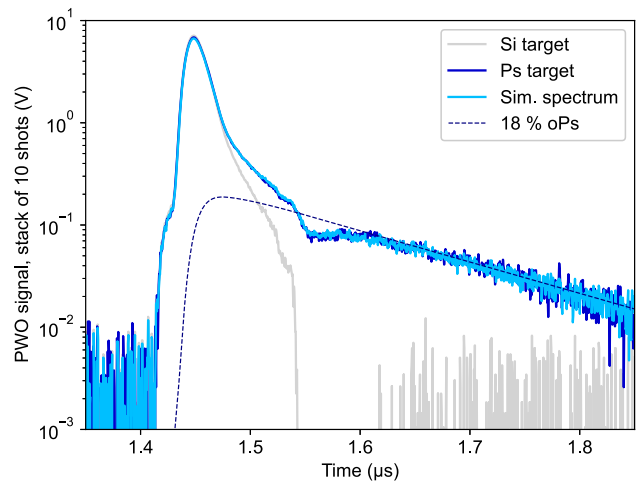


**Fig. 5** SSPALS spectrum obtained with a $PbWO_4$ crystal. The dip at 1.55 μs is due to the detector response. The data from the Si (grey) target is used to generate a template SSPALS (light blue) including ortho positronium formation and decay. An oPs fraction of 18% (dashed) provides a good fit for the experimental data of the mesoporous silica target (dark blue)

## 4 Antiproton beam

We use a drift tube to decelerate the antiprotons from 100 keV, as received from ELENA, to energies below 10 keV, suitable for $\bar{p}$ trapping and producing antihydrogen [19]. This tube can be held at high voltage, up to 100 kV, for 3 s before the antiproton bunch arrives, and is then switched to ground in 18 ns while the particles are inside. A leakage current varying between 10 and 30 μA on a 5 MΩ resistor leads to a voltage drop between 50 and 150 V that modifies the final beam energy. With a high voltage setting at 94 kV, the decelerated beam has an average energy of $6.10 \pm 0.05$ keV.

During the 2022 run, the intensity at extraction from ELENA was progressively increased from about $5 \times 10^6$ to about $7 \times 10^6$ $\bar{p}$ per bunch. The absolute accuracy of those values is of the order of 20%. Thanks to bunch rotation [27,28] performed in ELENA, the 100 keV antiproton bunch has a length of 40 ns (RMS) and a time-jitter of 4 ns. With these values, the bunch is well contained in the 450 mm long deceleration drift tube. This means that practically 100% of the $\bar{p}$ bunch is decelerated. The bunch rotation implies a doubling of the energy spread, up to $2 \times 10^{-3}$, but this has a negligible impact. The horizontal and vertical emittances were carefully measured by the ELENA team as 2.9 and 2.1 mm × mrad (RMS) respectively. These values are about 2.5 times larger than design, with a significant effect on the decelerated beam size and on the possibility to focus it at the point of reaction with the Ps. The bunch length after deceleration is 100 ns (RMS). ELENA also enabled the delivery of 100 keV $H^-$ ions every 15 s that were used to perform a first adjustment of the electrostatic optical elements of the beam line. Plastic scintillator detectors are placed along the beam line. Their time resolution of a few ns allows to locate the places where antiprotons annihilate and helps adjusting the voltages of the optical elements (steerers and Einzel lenses) to optimise $\bar{p}$ transmission (Fig. 6).

A SIMION® 8.1 [29] simulation, interfaced with COMSOL® [30] field maps, models the transport and focussing elements of the $\bar{p}$ beam to the reaction chamber. This simulation, using the 100 keV ELENA beam parame-

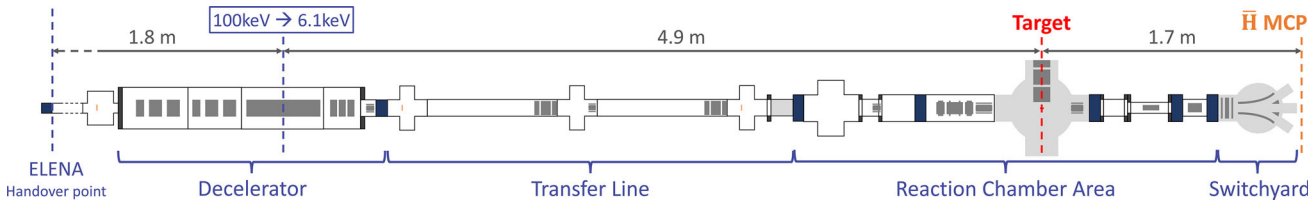


**Fig. 6** GBAR $\bar{p}$ beam line in 2022. The beam is decelerated by the drift tube, then focussed in the reaction chamber where it meets the Ps target to form $\bar{H}$ atoms. After the RC an electrostatic switchyard can deflect the $\bar{p}$ beam to the ion beamline, where a $\bar{p}$ trap (not shown) is currently located. For the $\bar{H}$ formation experiment, the deflector located right after the reaction region removes most of the $\bar{p}$s, while the switchyard removes the remaining ones. The neutral atoms are detected in the $\bar{H}$ MCP located in straight line downstream

ters, allows to estimate that the fraction of the $\bar{p}$ bunch that intersects the 5 mm collimator located after the Ps converter in the RC is 38%. The divergence of the neutral beam results in a fraction of the particles not hitting the $\bar{H}$ MCP, with an estimated loss of 32%.

Beam bunches of typically a few $10^6$ antiprotons can be examined by the $\bar{H}$ MCP at low gain settings in special runs where the deflectors after the target are not activated. The 2D image and the electric signal are simultaneously recorded (for the latter see Fig. 9). The $\bar{H}$ MCP detection system can also be operated at high gain for single-particle detection and is described in detail in Sect. 5. The determination of $\bar{p}$ numbers (per bunch), using the electrical and optical signals directly from the MCP, are not reliable due to the uncertainty on the gain (varying also locally) and the complexity of the determination of the ionisation yield for $\bar{p}$ annihilations at the MCP surface. For a better measurement a commercial digital camera [31] without the lens was placed outside the beam pipe at a distance of about 30 cm above the MCP to record the energy deposits of charged annihilation products in its CMOS sensor in a particle tracking mode. Thanks to the large number of pixels (5 M) and a detection efficiency close to 100%, the sensor can reliably count charged particle tracks in the high density environment generated by the annihilation of millions of antiprotons. The number of annihilations is inferred from the number of adjacent pixel clusters (tracks), taking into account the number and nature of annihilation products per antiproton, which depends on the nature of the target atoms [32], and the effect of material between the target and the sensor, derived from a simple GEANT4 model [33]). The uncertainty of the method is estimated to be around ±25% mainly due to different materials on the MCP surfaces and a rough assessment of the effect of the material of the beam pipe.

The number of antiprotons reaching the $\bar{H}$ MCP, with the $\bar{p}$ deflection electric fields off (see Sect. 5), is determined to be about $2.3 \times 10^6$ per spill. Taking into account a transmission efficiency of 74%, from simulation, we estimate the number of antiprotons passing through the positronium cloud to be about $3.1 \times 10^6$ per spill on average. This number and the number of positroniums obtained in the previous section serve as inputs to estimate the expected number of antihydrogen atoms produced according to reaction (1) as described in the following section.

## 5 $\bar{H}$ production measurement

The parts of the experiment where the creation of antihydrogen and its detection take place are shown schematically in Fig. 7. The antiprotons are focussed at the target location where they meet the positronium cloud. The antiprotons that did not react and emerge from the Ps cloud are directed towards the walls of the RC by applying a voltage on an electrostatic deflector whose 5 mm diameter aperture acts as collimator (see Fig. 4). The neutrals fly undeflected towards the $\bar{H}$ MCP detector located on the $\bar{p}$ beam axis 1.7 m downstream of the Ps target. In case that some antiprotons, for instance from the beam halo, survive the deflector, the electric field in the switchyard electrodes deviates them towards a beam line at 35 degrees from the main axis.

The $\bar{H}$ MCP is composed of a set of two Micro Channel Plates in chevron configuration from Photonis (Advanced Performance Detector model), with a gain of $1.76 \times 10^7$, at 2200 V, followed by a fast P46 phosphor screen (about 100 ns decay time). The MCP has a diameter of 40 mm and a thickness of 1 mm. The signal from its front face is read with 50 Ω to ground by a fast digital oscilloscope triggered by the extraction signal from ELENA. The time resolution for a single particle is less than 2 ns. A camera, model pixelfly from PCO with Sony ICX285AL image sensor, with a resolution of 1392 × 1040 pixels, records the image from the phosphor screen with a shutter speed set at 1 $\mu s$.

To estimate the expected production of antihydrogen, the time evolution of Ps diffusing out of the silica target is taken into account as well as the time and spatial overlap of the interacting particles. Ps is assumed to be emitted from the target with a distribution corresponding to the implanted positron profile measured by the position sensitive MCP at the target position (see Fig. 4), which is well represented by a

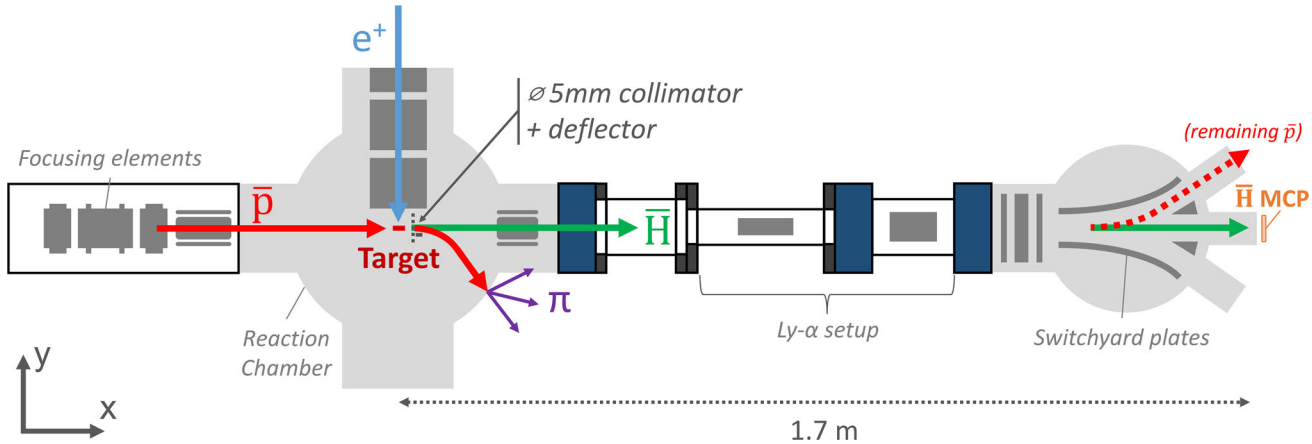


**Fig. 7** Illustration of the interaction region and the detection scheme for the resulting $\bar{H}$ atoms

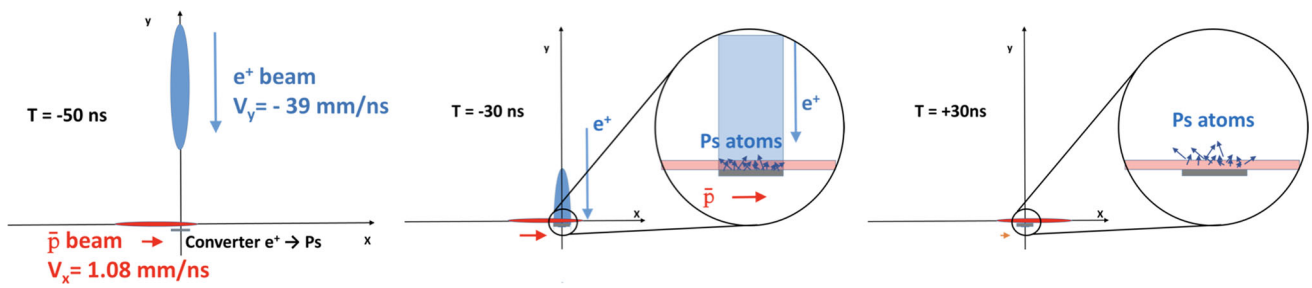


**Fig. 8** Scheme of the interaction seen from above. $e^+$ beam in blue, $\bar{p}$ beam in red. The ellipses show approximately the FWHM size. The $\bar{p}$ beam is almost symmetric (but not quite) transverse to its direction of propagation, i.e. in (Y,Z). The $e^+$ beam is flattened, i.e. narrower in the Z direction (height) and elongated in X. Note that the velocities of the two beams are very different. T = 0 is the time when the center of the $\bar{p}$ beam goes through the point x = 0. Left: T = − 50 ns before the interaction. No Ps has been produced yet. Center: T = − 30 ns, the $e^+$ beam has started impinging on the converter, producing Ps atoms which fly away slowly from the converter (velocity and angular distribution described in the text) Right: T = + 30 ns: the $e^+$ beam has completely passed. No more Ps is produced, but Ps atoms are still flying away from the converter. Note that on their way the Ps atoms can decay with a 142 ns lifetime

two dimensional profile of widths 3.5 and 0.5 mm along the antiproton beam axis and the vertical axis respectively. The positron pulse length is 17 ns (FWHM). The implantation energy of 4.3 keV in the nanoporous thin film results in a delay in the emission of oPs of 10 ns with 2 ns RMS [34].

The velocities of the Ps atoms can be described with a Maxwell-Boltzmann distribution with an average of 0.121 mm/ns emitted with a cosine distribution ($dn/dcos(\theta) \propto \cos(\theta)$) [35], as validated by experiments at ETH Zurich [36]. Figure 8 shows the principle of the $\bar{H}$ production. The expected antihydrogen production rate is obtained by calculating the space and time overlap of the $\bar{p}$ beam with the Ps cloud, taking into account the $\bar{p}$ and $e^+$ beam profile and motion, and the flight of the Ps atoms away from the converter and their decay time. A simple way of presenting this calculation is the following: $N_{\bar{H}} = N_{\bar{p}} \times N_{e^+} \times \epsilon_{e^+\to Ps} \times \sigma \times \frac{1}{A} \times I_{overlap}$ where $\epsilon_{e^+\to Ps}$ is the $e^+$ to Ps conversion efficiency, $\sigma$ the interaction cross-section, A the area of the interaction region transverse to the $\bar{p}$ direction (X-axis), and $I_{overlap}$ is a dimensionless quantity representing the space and time overlap efficiency. For our nominal conditions, the numbers are $3.07 \times 10^6$ $\bar{p}$, $3.9 \times 10^7$ $e^+$, $\epsilon_{e^+\to Ps} = 0.18$, $A = 0.2$ cm$^2$, and the overlap integral is $I_{overlap} = 0.076$.

The 5 mm diameter collimator located on the $\bar{p}$ beam axis 26 mm after the positron converter defines the transverse acceptance for the anti-atoms (Fig. 4). The target length along the antiproton axis and the collimator transverse to it, define the volume in which the Ps and $\bar{p}$ interact. The calculated cross section is dominated by 2P states which after production would decay promptly (1.6 ns) to the ground state. In the Close Coupling method [16] the predicted value is $13.4 \times 10^{-16}$ cm$^2$ at 6.1 keV incident $\bar{p}$ energy, while it is $30.6 \times 10^{-16}$ cm$^2$ in the Coulomb-Born approximation [15]. The expected production rates are $1.1 \pm 0.4$ $\bar{H}$ and $2.5 \pm 0.9$ $\bar{H}$ per 100 spills for the two models respectively, the uncertainty coming from the $\bar{p}$ flux and Ps number.

The data were taken from October to November 2022, in periods of 8 h shifts. The "MIX" periods combined the antiprotons with positronium (6897 spills), while the "BGD"

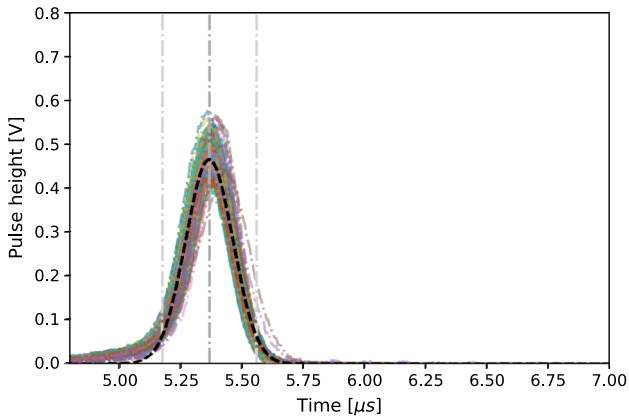


**Fig. 9** Electric signals of multiple $\bar{p}$ bunches on $\overline{H}$ MCP. The time profile of a single signal is generated by the longitudinal bunch profile and is well described by a Gaussian distribution with a 96 ns standard deviation. The spread in amplitude corresponds to the spread of the bunch intensities. The time walk (RMS 10 ns) is due partly to the jitter of the $\bar{p}$ bunches from ELENA and to fluctuations of the decelerated energy due to the limited stability of the drift tube decelerating voltage. The vertical lines define the signal time window taken for the analysis: $5.37 \pm 2 \times 0.096$ μs

data were taken without positrons (8468 spills). Data were also recorded with only positrons and no antiproton beam to study the background due to positron annihilation or Ps decay. Some data were also collected with no beam to ensure there were no backgrounds due to the environment and cosmic rays.

### 5.1 MCP electrical signal analysis

At 6.1 keV, the time of flight between the creation point in the reaction chamber and the detector is 1.6 μs. The bunch of antiprotons produces a signal of 96 ns width (RMS) on the $\overline{H}$ MCP when the electrostatic deflector is grounded, as shown in Fig. 9. A time interval of ±2 standard deviations around the central arrival time of these undeflected antiprotons (Fig. 9) is defined as the time span during which we accept $\overline{H}$ candidate events.

The time width of the recorded signals is typically smaller than 2 ns. Several such signals are recorded by the MCP per shot in the 10 μs time window of the data acquisition system. We define $V_{max}$ as the maximum voltage of an event and $T_{max}$ its associated time. Figure 10 left shows the scatter plot of $V_{max}$ versus $T_{max}$ for events in the MIX and BGD samples. In the MIX data there are clearly events with a large pulse height in the signal time-window, which are not present in the BGD data. This is what is expected for antihydrogen since in this case anti-atoms can reach and annihilate on the MCP while antiprotons are deflected and annihilate upstream, thus only pions can reach the MCP.

The gamma rays from oPs decay may also be a source of background. This is largely reduced with the selection of events in the signal window, corresponding to 10 lifetimes of oPs. Given the MCP solid angle and a detection efficiency of 5% that takes into account the high gain ($10^7$), a total of 18 such photons would have been detected. Considering the MCP efficiency, measured with photons from a $^{22}$Na source, of less than 1%, after a cut on $V_{max}$ at 0.05 V, this background is negligible.

Figure 10 right shows the distribution of $V_{max}$ for candidate events in the MIX and BGD runs in the signal window. Testing for the presence of a signal amounts to testing that the Poisson distributions which generated the MIX and BGD samples have the same average parameter. Let $N_{MIX}$ and $N_{BGD}$ be the total number of events and $n_{MIX}$ and $n_{BGD}$ the number of observed signal-like and background-like events. If they come from the same law, $n_{MIX}$ and $n_{BGD}$ should be shared along a binomial distribution whose parameter p is approximated by: $p = \frac{N_{MIX}}{N_{MIX}+N_{BGD}}$ [37]. The binomial test calculates the (two-sided) probability that the observed $n_{MIX}$ departs from its natural value $p \times (n_{MIX} + n_{BGD})$. This probability is then translated into a number of standard deviations by the usual formula for Gaussian distributions. The significance varies with the cut value between 3.1 and 4.1 standard deviations for cut values above 0.05 V.

For a minimum voltage cut of 0.1 V, the number of events in MIX and BGD shots are 32 and 15 respectively. The normalised background is $12.2 \pm 3$, i.e. an excess of $19.8 \pm 6$ with a significance of 3.1 standard deviations. The efficiency of the detection by the MCP for this cut value is estimated to be about 50%. The nominal acceptance of $\overline{H}$ atoms in the detection area of the MCP is estimated by simulation to be 68% (see Sect. 4). However we observed perturbations of the charged beam with respect to its nominal trajectory, which might impair the acceptance for the neutrals, hence this value can only be taken as an upper limit. Taking into account the number of shots in the MIX and BGD samples, and the efficiencies and acceptances described above, the excess in the MIX shots corresponds to $8.9 \times 10^{-3}$ $\overline{H}$ produced in the Ps target per antiproton pulse. Given the large uncertainty in the acceptance of $\overline{H}$ atoms, this is in rough agreement with the number between $1.1 \pm 0.4 \times 10^{-2}$ and $2.5 \pm 0.9 \times 10^{-2}$ $\overline{H}$ per antiproton pulse, expected from different theoretical models. In the future, several improvements will be brought to the control of the charged and neutral trajectories to enable a proper cross-section measurement.

### 5.2 MCP image analysis

A cross-check of the analysis can be performed using the MCP images recorded for the same spills. The MCP image for the impact of an $\overline{H}$ atom is expected to be similar to that for the impact of an antiproton. The images display individual impacts, however it is not possible to attribute both a precise timing and a precise charge to a single impact, since

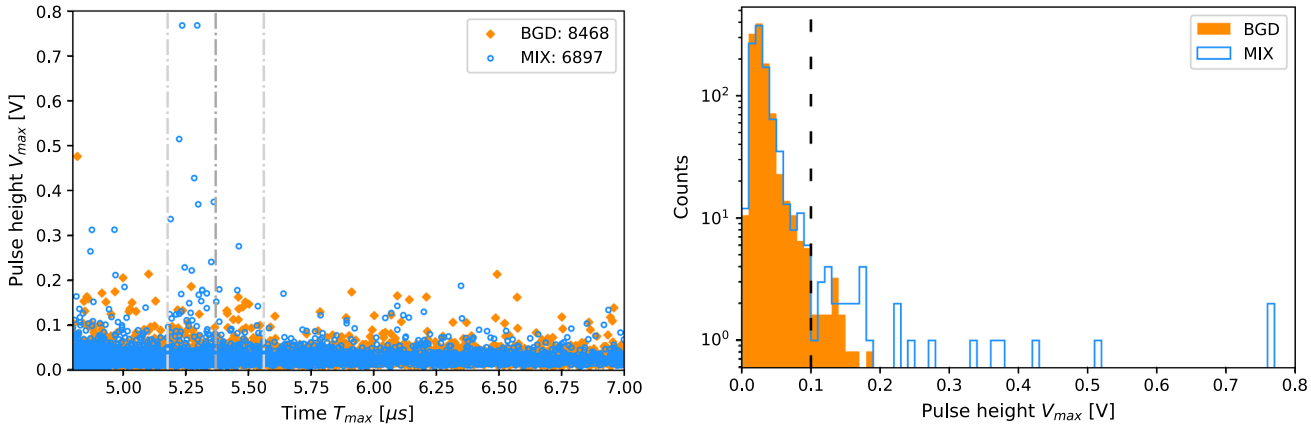


**Fig. 10** Left: Pulse-height ($V_{max}$) vs. time ($T_{max}$) distribution of MCP signals for MIX events (hollow blue) and for BGD events (orange). The vertical gray lines indicate the time-of-flight signal region where $\overline{H}$ atoms are expected to annihilate on the detector. Right: Pulse height ($V_{max}$) distribution of MIX events (blue) and BGD events (orange) in the signal time-interval. The BGD histogram is scaled to the number of MIX spills.The vertical dashed line indicates a separation for a cut value of 0.1 V

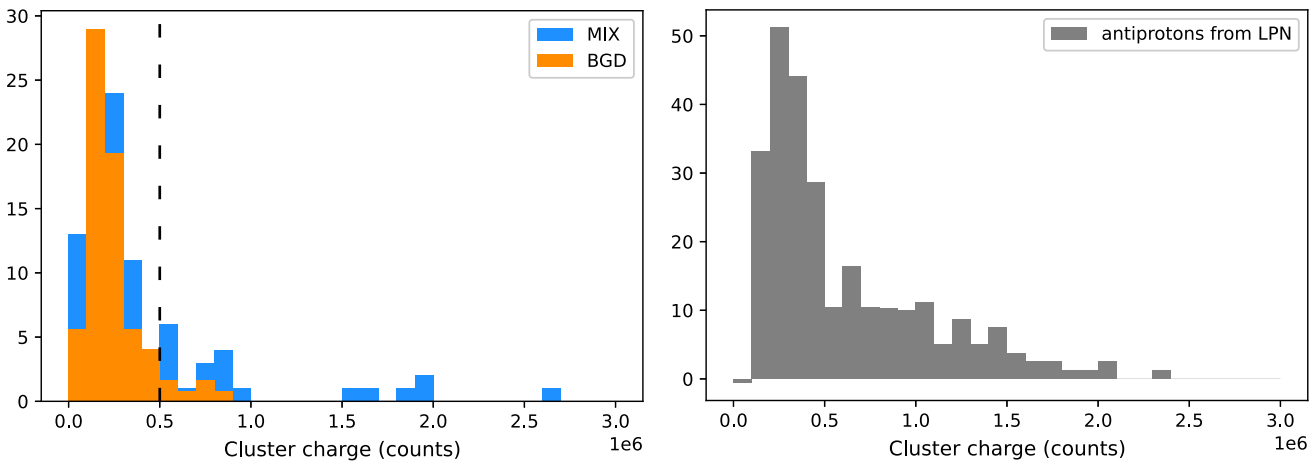


**Fig. 11** Distribution of cluster charge. Left: MIX and BGD shots, right: antiprotons (from LPN shots). The vertical dashed line indicates a separation for a cut value of $0.5 \times 10^6$ counts

the screen and the camera integrate over a time interval of 1 µs. This is in contrast with the electrical pulse from the MCP, used in the analysis above, which is very short but integrates over the whole MCP area. To characterize the image of these impacts, special runs (LPN, for low $\overline{p}$ number) were taken with a low number of antiprotons reaching the MCP, by detuning the incoming $\overline{p}$ beam. In these shots, the average hit multiplicity on the MCP is 7.5 with large fluctuations and containing a substantial number of pions produced by the annihilations of the antiprotons deflected upstream. The images are analysed with the help of a simple clustering algorithm. The charge of a cluster is defined as the sum of the collected charge from each pixel belonging to it. The distribution of the cluster charge for antiprotons is extracted from the difference between the distributions for LPN and Background runs and is shown in Fig. 11 (right). Images in the MIX and BGD samples are analysed with the same clustering algorithm. The resulting distributions of cluster charge are shown in Fig. 11 (left). The large charge events seen in the MIX sample have a cluster charge compatible to that expected from antiproton impacts, as extracted from the LPN data. A typical large-charge MIX event image is shown in Fig. 12. Selecting clusters of charge superior to $5 \times 10^5$ counts keeps 50% of them. Using this minimum value, the number of events in MIX and BGD runs are 22 and 6 respectively. The normalised background is $4.8 \pm 2$ i.e. an excess of $17.2 \pm 5.1$ events, with a significance of 3.6 standard deviations, similar to the results obtained with the electrical signal analysis.

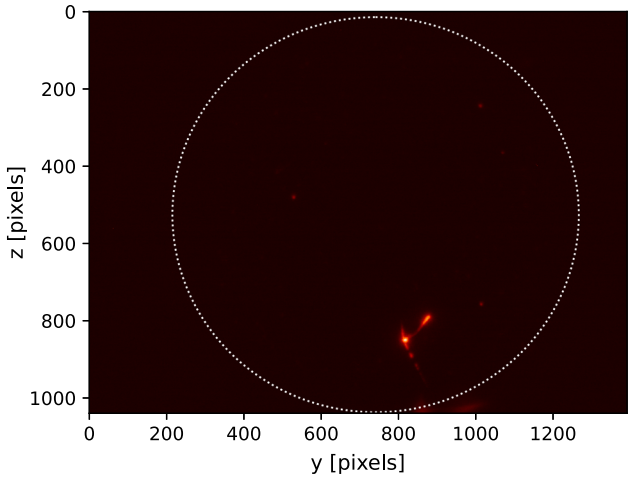


**Fig. 12** Example of MCP image for a large charge MIX event. The dotted circle represents the limit of the MCP active area

## 6 Summary and outlook

We have observed the production of antihydrogen atoms via charge exchange of 6.1 keV antiprotons with positronium atoms in the fundamental state.

Theory predicts most of these anti-atoms to be in the ground state while they travel through the Ps cloud, which is beneficial for the subsequent production of $\overline{\mathrm{H}}^+$ ions. In the future, GBAR intends to produce $\overline{\mathrm{H}}^+$, cool them to velocities of the order of $\sim 1$ ms$^{-1}$, and photo-neutralise them to obtain slow $\overline{\mathrm{H}}$ atoms. The free fall of these atoms could then be measured by a classical time/position measurement, or even more accurately by a quantum interference method [38]. The observed production of 6 keV $\overline{\mathrm{H}}$ atoms constitutes the first milestone of this roadmap. Furthermore, in the presently demonstrated scheme of $\overline{\mathrm{H}}$ production, a substantial fraction of the order of 15% of the anti-atoms should be in the 2S state, allowing to measure the Lamb shift of antihydrogen in different conditions from those of the previous measurement [39], in particular in a non-magnetic environment [40]. Such a measurement would be complementary with other efforts to search the CPT-violating parameter space for signs of new physics [41].

In order to achieve the production of anti-ions, the rate of $\overline{\mathrm{H}}$ production must be increased substantially. Several improvements are being considered on the positron line, such as reaching the full power of the linac, optimising the positron moderator geometry, implementing a new trapping scheme in the BGT by replacing the $N_2$ gas by a solid state SiC re-moderator [42], and working on the transfer efficiencies between devices. On the antiproton line, a Penning trap has been added after the drift tube decelerator, with the possibility of electron-cooling and emitting bunches of cold antiprotons. This will largely improve the flux and emittance of the $\overline{\mathrm{p}}$ beam and allow to use a Ps confining cavity.

**Acknowledgements** We thank F. Butin and the CERN EN team, L. Ponce and the AD/ELENA team for their fruitful collaboration. A. Prost and T. Stadlbauer from CERN and D. C. Faircloth from RAL are also warmly thanked for their help on HV techniques for the decelerator as well as A. Sinturel for help and expertise on vacuum. We recall the help of A. Leite and A. Husson for their work during the commissioning phase of the experiment. This work is supported by: JSPS KAKENHI Grant-in-Aid for Scientific Research A 20H00150 and Fostering Joint International Research A 20KK0305 (Japan), ANTION ANR-14-CE33-0008 (France), Programme National Gravitation, Références, Astronomie, Métrologie (PNGRAM), Institut de Physique, CNRS (France), the Swiss National Science Foundation (Switzerland) grants 197346 and 216673 and ETH Zurich (Switzerland) grant ETH-46 17-1, the Swedish Research Council (VR) grants 2017-03822 and 2021-04005 and the following grants from Korea: IBS-R016-Y1, IBS-R016-D1, UBSI Research Fund (No. 1.220116.01) of UNIST, NRF-2016R1A5A1013277, NRF- RS-2022-00143178, NRF-2021R1A2C3010989, and NRF-2016R1A6A3A11932936. The GBAR collaboration is an International Research Network, supported by CNRS, France.

**Data Availability Statement** This manuscript has no associated data or the data will not be deposited. [Authors' comment: The datasets generated during the current study are available from the corresponding author on reasonable request.]

**Open Access** This article is licensed under a Creative Commons Attribution 4.0 International License, which permits use, sharing, adaptation, distribution and reproduction in any medium or format, as long as you give appropriate credit to the original author(s) and the source, provide a link to the Creative Commons licence, and indicate if changes were made. The images or other third party material in this article are included in the article's Creative Commons licence, unless indicated otherwise in a credit line to the material. If material is not included in the article's Creative Commons licence and your intended use is not permitted by statutory regulation or exceeds the permitted use, you will need to obtain permission directly from the copyright holder. To view a copy of this licence, visit http://creativecommons.org/licenses/by/4.0/.
Funded by SCOAP$^3$. SCOAP$^3$ supports the goals of the International Year of Basic Sciences for Sustainable Development.

## References

1. J. Walz, T. Hänsch, A proposal to measure antimatter gravity using ultracold antihydrogen atoms. Gen. Relativ. Gravit. **36**, 561 (2004). https://doi.org/10.1023/B:GERG.0000010730.93408.87
2. G. Chardin et al., GBAR Proposal to the 2011 CERN SPSC. http://cds.cern.ch/record/1386684/files/SPSC-P-342.pdf
3. G. Baur, Production of antihydrogen. Phys. Lett. B **368**, 251 (1996). https://doi.org/10.1016/0370-2693(96)00005-6
4. G. Blanford, Observation of atomic antihydrogen. Phys. Rev. Lett. **80**, 3037 (1996). https://doi.org/10.1103/PhysRevLett.80.3037
5. M. Amoretti, Production and detection of cold antihydrogen atoms. Nature **419**, 456 (2002). https://doi.org/10.1038/nature01096
6. G. Gabrielse, Background-free observation of cold antihydrogen with field-ionization analysis of its states. Phys. Rev. Lett. **89**, 213401 (2002). https://doi.org/10.1103/PhysRevLett.89.213401
7. G.B. Andresen et al. [ALPHA Collaboration], Trapped antihydrogen. Nature **468**, 673 (2010). https://doi.org/10.1038/nature09610
8. Y. Enomoto, Synthesis of cold antihydrogen in a cusp trap. Phys. Rev. Lett. **105**, 243401 (2010). https://doi.org/10.1103/PhysRevLett.105.243401

9. N. Kuroda, A source of antihydrogen for in-flight hyperfine spectroscopy. Nat. Commun. **5**, 3089 (2014). https://doi.org/10.1038/ncomms4089
10. M. Ahmadi, Antihydrogen accumulation for fundamental symmetry tests. Nat. Commun. **8**, 681 (2017). https://doi.org/10.1038/s41467-017-00760-9
11. C.H. Storry, First laser-controlled antihydrogen production. Phys. Rev. Lett. **93**, 263401 (2004). https://doi.org/10.1103/PhysRevLett.93.263401
12. C. Amsler, Pulsed production of antihydrogen. Commun. Phys. **4**, 19 (2021). https://doi.org/10.1038/s42005-020-00494-z
13. J.P. Merrison, Hydrogen formation by proton impact on positronium. Phys. Rev. Lett. **78**, 2728 (1997). https://doi.org/10.1103/PhysRevLett.78.2728
14. P. Comini, P.-A. Hervieux, $\overline{\mathrm{H}}^{+}$ ion production from collisions between antiprotons and excited positronium: cross sections calculations in the framework of the GBAR experiment. N. J. Phys. **15,** 095022 (2013). https://doi.org/10.1088/1367-2630/15/9/095022 [Corrigendum: P. Comini, P-A. Hervieux and K. Lévêque-Simon, N. J. Phys. **23**, 029501 (2021) https://doi.org/10.1088/1367-2630/abe2c1]
15. K. Lévêque-Simon, P.-A. Hervieux, Antihydrogen formation from laser-assisted antiproton-positronium collisions. Phys. Rev. A **107**, 052813 (2023). https://doi.org/10.1103/PhysRevA.107.052813
16. C.M. Rawlins, A.S. Kadyrov, A.T. Stelbovics, I. Bray, M. Charlton, Calculation of antihydrogen formation via antiproton scattering with excited positronium. Phys. Rev. A **93**, 012709 (2016). https://doi.org/10.1103/PhysRevA.93.012709
17. T. Yamashita, Near-threshold production of antihydrogen positive ion in positronium-antihydrogen collision. N. J. Phys. **23**, 012001 (2021). https://doi.org/10.1088/1367-2630/abd682
18. W. Bartmann, The ELENA facility. Philos. Trans. R. Soc. A **376**, 20170266 (2017). https://doi.org/10.1098/rsta.2017.0266
19. A. Husson, A pulsed high-voltage decelerator system to deliver low-energy antiprotons. Nucl. Instrum. Methods Phys. Res. A **1002**, 165245 (2021). https://doi.org/10.1016/j.nima.2021.165245
20. M. Charlton, Positron production using a 9 MeV electron linac for the GBAR experiment. Nucl. Inst. Methods Phys. Res. A **985**, 164657 (2021). https://doi.org/10.1016/j.nima.2020.164657
21. P. Blumer, Positron accumulation in the GBAR experiment. Nucl. Instrum. Methods Phys. Res. A **1040**, 167263 (2022). https://doi.org/10.1016/j.nima.2022.167263
22. Pre-amplifier model CSPA12-2S from FAST ComTec GmbH
23. D.A. Cooke, Positron extraction to an electromagnetic field free region. J. Phys. B **49**, 014001 (2015). https://doi.org/10.1088/0953-4075/49/1/014001
24. L. Liszkay, Positronium reemission yield from mesostructured silica films. Appl. Phys. Lett. **92**, 063114 (2008). https://doi.org/10.1063/1.2844888
25. P. Crivelli, Measurement of the orthopositronium confinement energy in mesoporous thin films. Phys. Rev. A **81**, 052703 (2010). https://doi.org/10.1103/PhysRevA.81.052703
26. D.B. Cassidy, S.H.M. Deng, H.K.M. Tanaka, A.P. Mills Jr., Single shot positron annihilation lifetime spectroscopy. Appl. Phys. Lett. **88**, 194105 (2006). https://doi.org/10.1063/1.2203336
27. R. Garoby, RF gymnastics in synchrotrons, 431. CERN Yellow Report CERN-2011-007. https://doi.org/10.48550/arXiv.1112.3232
28. J. Griffin et al., Time and momentum exchange for production and collection of intense antiproton beams at Fermilab. IEEE Trans. Nucl. Sci. **NS-30 No. 4** (1983)
29. D.A. Dahl, Simion for the personal computer in reflection. Int. J. Mass Spectrom. **200**, 3 (2000). https://doi.org/10.1016/S1387-3806(00)00305-5
30. Comsol multiphysics® v. 6.1. http://www.comsol.com. COMSOL AB, Stockholm
31. Camera model VCXG-51M from Baumer GmbH
32. G. Bendiscioli, D. Kharzeev, Antinucleon-nucleon and antinucleon-nucleus interaction. A review of experimental data. La Rivista del Nuovo Cimento **17**, 1 (1994). https://doi.org/10.1007/BF02724447
33. Geant4 a simulation toolkit. Nucl. Instrum. Methods Phys. Res. A **506**(3), 250 (2003). https://doi.org/10.1016/S0168-9002(03)01368-8
34. A. Deller, Positronium emission from mesoporous silica studied by laser-enhanced time-of-flight spectroscopy. N. J. Phys. **17**, 043059 (2015). https://doi.org/10.1088/1367-2630/17/4/043059
35. D.B. Cassidy, P. Crivelli, T.H. Hisakado, L. Liszkay, V.E. Meligne, P. Perez, H.W.K. Tom, A.P. Mills, Positronium cooling in porous silica measured via doppler spectroscopy. Phys. Rev. A **81**, 012715 (2010). https://doi.org/10.1103/PhysRevA.81.012715
36. M.W. Heiss, Precision spectroscopy of positronium using a pulsed slow positron beam, Doctoral Thesis (ETH Zurich, Zurich, 2021). https://doi.org/10.3929/ethz-b-000477081
37. J. Przyborowski, H. Wilenski, Homogeneity of results in testing samples from Poisson series: with an application to testing clover seed for dodder. Biometrika **31**, 313 (1940). https://doi.org/10.1093/biomet/31.3-4.313
38. O. Rousselle, Analysis of the timing of freely falling antihydrogen. N. J. Phys. **24**, 033045 (2022). https://doi.org/10.1088/1367-2630/ac5b57
39. M. Ahmadi, Investigation of the fine structure of antihydrogen. Nature **578**, 375 (2020). https://doi.org/10.1038/s41586-020-2006-5
40. P. Crivelli, D. Cooke, M.W. Heiss, Antiproton charge radius. Phys. Rev. D **94**, 052008 (2016). https://doi.org/10.1103/PhysRevD.94.052008
41. V.A. Kostelecký, A.J. Vargas, Lorentz and *cpt* tests with hydrogen, antihydrogen, and related systems. Phys. Rev. D **92**, 056002 (2015). https://doi.org/10.1103/PhysRevD.92.056002
42. A.M.M. Leite, P. Debu, P. Pérez, J.-M. Reymond, Y. Sacquin, B. Vallage, L. Liszkay, Efficient positron moderation with a commercial 4h-sic epitaxial layer. J. Phys. Conf. Ser. **791**, 012005 (2017). https://doi.org/10.1088/1742-6596/791/1/012005